ACS OMEGA

http://pubs.acs.org/journal/acsodf

Article

Improving the GaN Growth Rate by Optimizing the Nutrient Basket Geometry in an Ammonothermal System Based on Numerical Simulation

Pengfei Han, Bing Gao,* Botao Song, Yue Yu, Xia Tang, and Sheng Liu

Cite This: *ACS Omega* 2022, 7, 9359−9368

Read Online

ACCESS | Metrics & More | Article Recommendations

ABSTRACT: The low growth rate of bulk gallium nitride (GaN) when using the ammonothermal method is improved herein by optimizing the nutrient geometry. A numerical model considering the dissolution and crystallization process is developed. Heater powers are employed as thermal boundary conditions to match the real ammonothermal system. The flow field, thermal field, and mass concentration field in the autoclave are calculated with or without a central hole in the nutrient basket. Numerical results show that the mass transfer efficiency and supersaturation on the seed crystal surface can be improved with a hole in the nutrient basket in the center in spite of its diverse effect on the heat transfer, which can be overcome by adjusting the heater powers. As a result, the growth rate of the GaN crystal can be obviously increased.

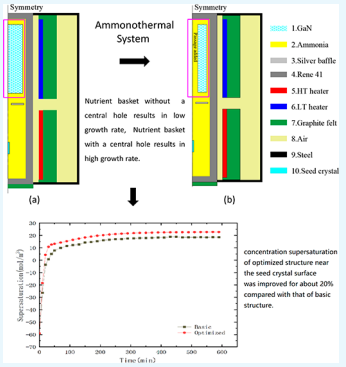

1. INTRODUCTION

In recent years, gallium nitride (GaN) has been widely used in wireless charging, inverter technology, 5G communication, and radar fabrication, especially for high-power and high-frequency electronic devices,[1,2] due to its wide band gap. The broad use of GaN has accelerated the study of GaN growth using different methods.[3] Today, GaN is mainly grown using three methods: the hydride vapor phase epitaxy (HVPE) method, the sodium flux method (Na-flux method),[4] and the ammonothermal method.[5] The ammonothermal method can provide GaN substrates with the lowest thread dislocation density (TDD).[6] Therefore, the ammonothermal method is considered to be the most promising way of fabricating bulk GaN crystals with high quality.

Several groups have reported results on GaN crystal growth using ammonothermal experiments. Zajac et al.[7] grew a 2 in. GaN crystal with a curvature radius of tens of meters, obtaining a TDD on the order of 5×10^4 cm^{-2}. Pimputkar et al.[8] obtained high-purity GaN crystals on HVPE seeds by placing a silver capsule into an autoclave. Schimmel et al.[9] detected the formation and transport of Ga-containing intermediates using an X-ray transmission monitoring tool. There are also several companies engaged in high-quality GaN growth in a basic or acidic ammonothermal system, such as Ammono (basic environment), SixPoint Materials Inc. (basic),[10] Mitsubishi Chemical Corp. (Japan; acidic), Soraa, Inc. (high-temperature acidic),[11,12] Asahi Kasei Corp. (acidic).[13]

Numerical simulations have also been used to study the ammonothermal method. Chen and his co-workers[14−16] model the full ammonothermal growth processes for the first time using fluid dynamics, thermodynamics, and heat-transfer models. They use the constant temperatures for the high and low temperature heaters to keep the temperature difference at 50 °C. The Grashof number and Prandtl number in their study are Gr = 6.0×10^7 and Pr = 0.73, respectively. The influence of the baffle opening on the mass transfer has been numerically analyzed. Calculation results show that the baffle opening has a significant influence on the temperature difference as well as the flow and heat transfer in the autoclave. Masuda et al.[17] numerically study the flow and temperature field with funnel-shaped baffles inside an autoclave. In their study, constant temperature is used as a thermal boundary condition, of which the high and low temperatures are 420 and 400 °C. The flow region is calculated using the k-ε model. The Boussinesq approximation is employed to calculate the natural convection. They found that the optimum angle of the funnel-shaped baffle is 20°. Mirzaee[18] introduces the reaction kinetics and Piecewise Linear Interface Calculation (PLIC) method in his ammonothermal model and illuminates the effect of a narrow gap between the nutrient basket and autoclave wall on the growth of GaN. The lower and

Received: November 10, 2021
Accepted: February 24, 2022
Published: March 10, 2022

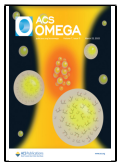

https://doi.org/10.1021/acsomega.1c06154
ACS Omega 2022, 7, 9359−9368

upper external sidewalls in their study are maintained at the constant temperatures of 525 and 475 °C. The ammonothermal system used in their study is based on the model developed by Chen. Schimmel et al.[19] numerically study the effect of heat conduction and convection on the possible measurement error during experiments. In their study, they conduct several simulations of thermocouple heating using the SIMPLEST algorithm. The Rayleigh numbers of their study are among $(2.88-5.69) \times 10^7$; results of experiment and simulation show that fluid flow in the autoclave has a significant effect on the temperature distribution. Enayati et al.[20,21] develop a three-dimensional (3D) model to simulate the flow and heat transfer in an ammonothermal crystal growth reactor. Water is used as the flow media. The Rayleigh number of their study is 8.8×10^6, and constant temperatures of 303.15 and 296.15 K in the lower and upper halves are imposed as the thermal condition. The effect of reactor size, rack, and seeds on the flow and heat transfer are analyzed based on their results.

The low growth rate of the ammonothermal method is a main challenge for its extensive industrial application. Many studies have been performed to improve the growth rate. However, most of them concentrated on the baffle opening and the location of heaters. The shape influence of the porous nutrient basket has mostly been ignored. One study[18] showed a potentially significant impact of a porous nutrient basket on the mass transfer between the porous and free-flow areas.

In this study, numerical simulations by COMSOL multiphysics are used to improve the growth rate of GaN by optimizing the nutrient basket shape in the ammonothermal system.

2. PROCESS AND MODEL DESCRIPTION

2.1. Geometric Model. The autoclave is set to be axisymmetric considering a cylindrical seed crystal. The low- and high-temperature areas are maintained around suitable temperatures by the low-temperature (LT) heater (component 6) and high-temperature (HT) heater (component 5), respectively. The LT heater is located in the upper region, whereas the HT heater is located in the lower region. They are coated with graphite felt (component 7). A silver baffle (component 3) containing a center opening with 5% of the total area is placed in the middle of the chamber to increase the temperature gradient. The gap between the baffle and autoclave is 5% of the diameter of the autoclave. KNH_2 is used as a mineralizer in the model, resulting in the retrograde solubility of the system. The GaN nutrient basket (component 1) is located in the upper region, while the seed crystal (component 10) is located in the lower region. The gap between the nutrient basket and the autoclave wall is 1 mm. The autoclave wall is made of Rene 41 (component 4), and the shell is made of stainless steel (component 9). The yellow region in the autoclave represents the supercritical ammonia (component 2). The area among the autoclave, heaters, graphite felt, and the shell is filled with air (component 8).

Figure 1a shows the basic schematic structure of the ammonothermal autoclave, and Figure 1b shows the optimized structure with a 2 mm hole in the center of the nutrient basket. Since the temperature variation is narrow, the values of ammonia and GaN physical properties varied little upon pressure, and they are acquired from ref 18.

The main geometry size of the autoclave is illustrated in Figure 2.

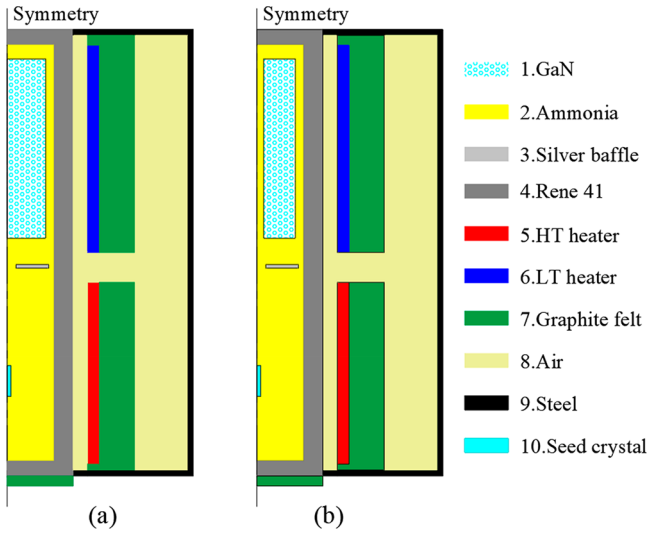

Figure 1. (a) Schematic diagram of a basic ammonothermal autoclave. (b) Schematic diagram of an optimized ammonothermal autoclave.

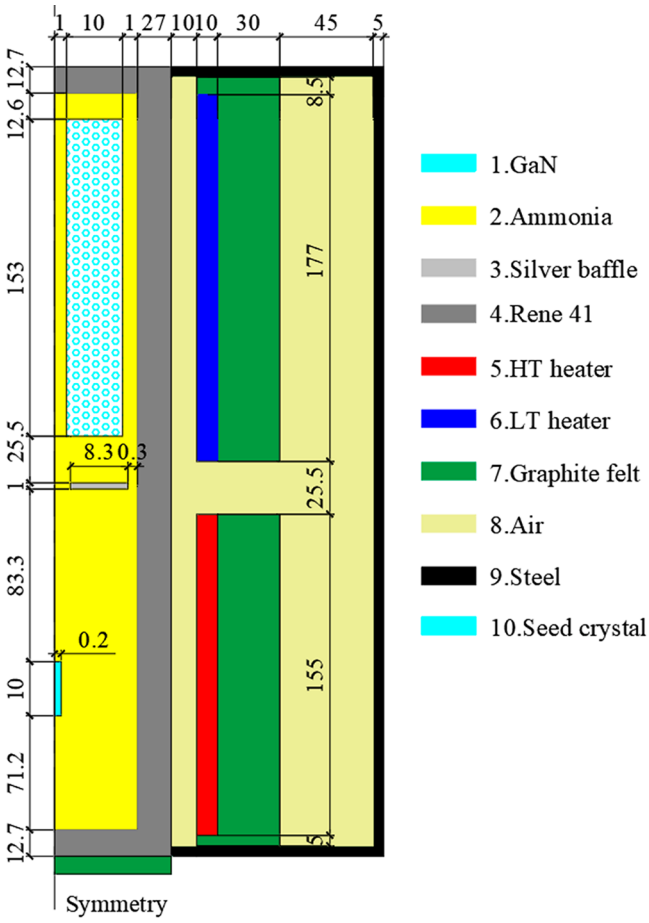

Figure 2. Geometry size of the autoclave (units: mm).

2.2. Governing Equations. The governing equations of flow include the Navier–Stokes equation in the free fluid flow region and the Brinkman equation in the porous region (equations 1 and (2)). To reduce the nonlinearity when solving the flow governing equations, the Boussinesq approximation is employed. The porosity ε is 1 for the free flow region and 0.4 for the porous region.

https://doi.org/10.1021/acsomega.1c06154
ACS Omega 2022, 7, 9359−9368

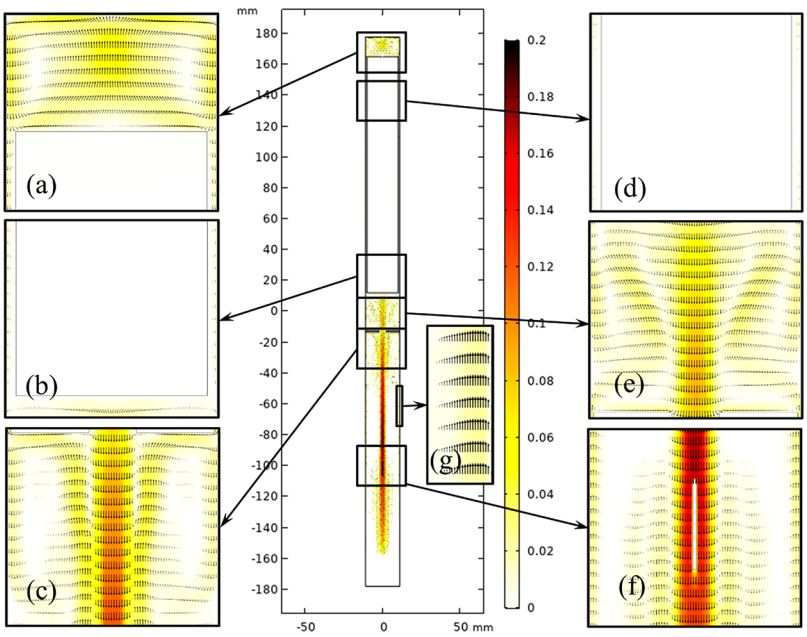

Figure 3. Velocity vector distribution in the chamber of the basic autoclave structure. (a) Part 1. (b) Part 2. (c) Part 3. (d) Part 4. (e) Part 5. (f) Part 6. (g) Boundary layer capture.

$$\frac{\partial(\varepsilon\rho_f)}{\partial t} + \nabla\cdot(\rho_f\mathbf{u}) = 0 \tag{1}$$

$$\rho_f\frac{\partial\mathbf{u}}{\partial t} + \frac{\rho_f}{\varepsilon}\mathbf{u}\cdot\nabla\mathbf{u} = -\nabla p + \mu_f\nabla^2\mathbf{u} - B\left[\frac{\varepsilon\mu_f}{\lambda} + \frac{\varepsilon\rho_f C_E}{\sqrt{\lambda}}|\mathbf{u}|\right]\mathbf{u} - \varepsilon\rho_{ref}\mathbf{g}\beta(T - T_{ref}) \tag{2}$$

Here, ρ_f is the fluid density, $\mathbf{u}$ is the fluid velocity, ε is the porosity, λ is the permeability, C_E is the Forchheimer coefficient, μ_f is the fluid viscosity, ρ_{ref} is the reference density, T is the fluid temperature, T_{ref} is the reference temperature, β is the volume expansion coefficient, and the value of g is 9.8 kg·m/s^2. B is considered 1 for the free flow region and 0 for the porous region.

The temperature field is calculated using the energy equation. Equations 3 and (4) represent the energy equation in the free flow and porous fields, respectively. The heat transfer of the solid components is calculated using Equation 5. The radiation heat transfer is expressed using eqs 6 and (7). The heat transfer and radiation couple with each other.

$$\frac{\partial(\rho c_p T)}{\partial t} + \nabla\cdot(\rho c_p T\mathbf{u}) = \nabla\cdot(k\nabla T) \tag{3}$$

$$\frac{\partial((\rho c_p)_{eff}T)}{\partial t} + \nabla\cdot(\rho c_{p,f}T\mathbf{u}) = \nabla\cdot(k_{eff}\nabla T) + Q_s \tag{4}$$

$$\rho c_{p,s}\frac{\partial T}{\partial t} + \nabla(-k\nabla T) = Q \tag{5}$$

$$J_i - (1 - \varepsilon_i)\sum_j F_{ij}J_j = \varepsilon_i E_{b,i} \tag{6}$$

$$\frac{q_i}{A_i} = \varepsilon_i\left(E_{b,i} - \sum_j F_{ij}J_j\right) \tag{7}$$

Here, c_p is the heat capacity, T is the temperature, k is the heat conductivity coefficient, and Q is the heat source. The subscript eff represents the effective value in the porous region, whereas f and s represent fluid and solid, respectively. J_i is the radiosity, ε_i is the emissivity, F_{ij} is the view factor, $E_{b,i}$ is the emissive power of a blackbody, and q/A is the heat flux.

The mass transfer of metastable GaN can be calculated using the convective−diffusive equation. Equation 8 expresses the mass transfer mechanism in the free flow field. Considering the porosity and mass solution in the porous area, the mass transfer equation is transformed to Equation 9.

$$\frac{\partial(\rho C)}{\partial t} + \nabla\cdot(\rho C\mathbf{u}) = \nabla\cdot(D\nabla(\rho C)) \tag{8}$$

$$\rho_f\varepsilon\frac{\partial(C_f)}{\partial t} + \rho\mathbf{u}\nabla\cdot(C_f) = \rho_f D_{eff}\nabla^2(C_f) + \phi_c \tag{9}$$

Here, C and C_f represent the species concentration, and D represents the diffusion coefficient. ϕ_c is the mass source.

The dissolution and crystallization reactions are shown in Equations 10 and (11). The mass resource of dissolution and crystallization can be calculated as a function of the concentration gradient and chemical kinetics (Equation 12).[19]

$$(KNH_2 + NH_3)_{solvent} + GaN_{solid} \rightarrow KGa(NH_2)_{4metastable} \tag{10}$$

$$KGa(NH_2)_{4metastable} \rightarrow (KNH_2 + NH_3)_{solvent} + GaN_{solid} \tag{11}$$

$$\phi_c = \frac{1}{\forall}[\rho_f\kappa A_{fs}(C_{max} - C_f)] \tag{12}$$

Here, $A_{fs}/\forall$ is the surface-to-volume fraction, and κ is the reaction rate coefficient, the value of which is 10^{-6} m/s,[18,22] and C_{max} is the maximum species concentration under certain temperature.

Data obtained from literature[25] show that the solubility (mass fraction) of metastable GaN decreases with the increasing temperature. The relationship between C_{max} and temperature can be expressed as Equation 13.

https://doi.org/10.1021/acsomega.1c06154
ACS Omega 2022, 7, 9359−9368

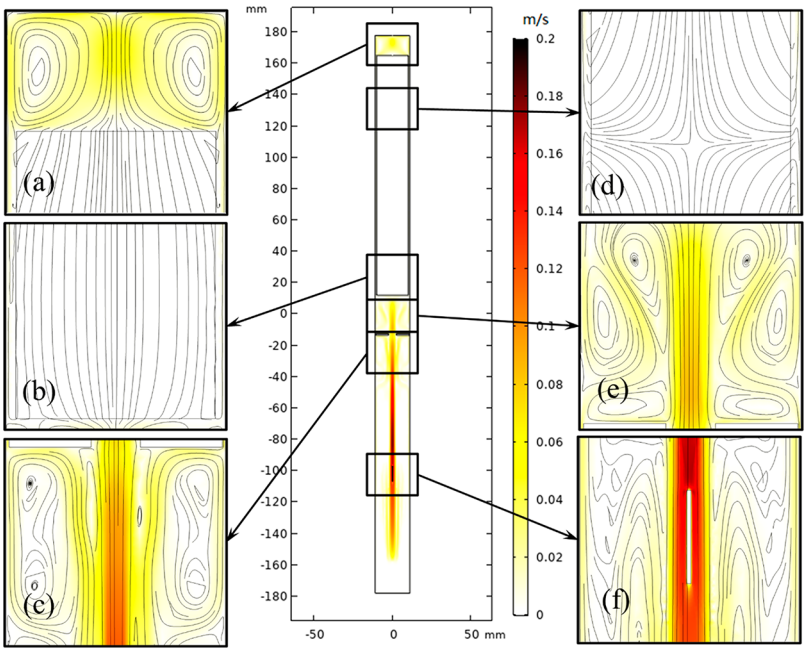

Figure 4. Streamline distribution in the chamber of the basic autoclave structure. (a) Part 1. (b) Part 2. (c) Part 3. (d) Part 4. (e) Part 5. (f) Part 6.

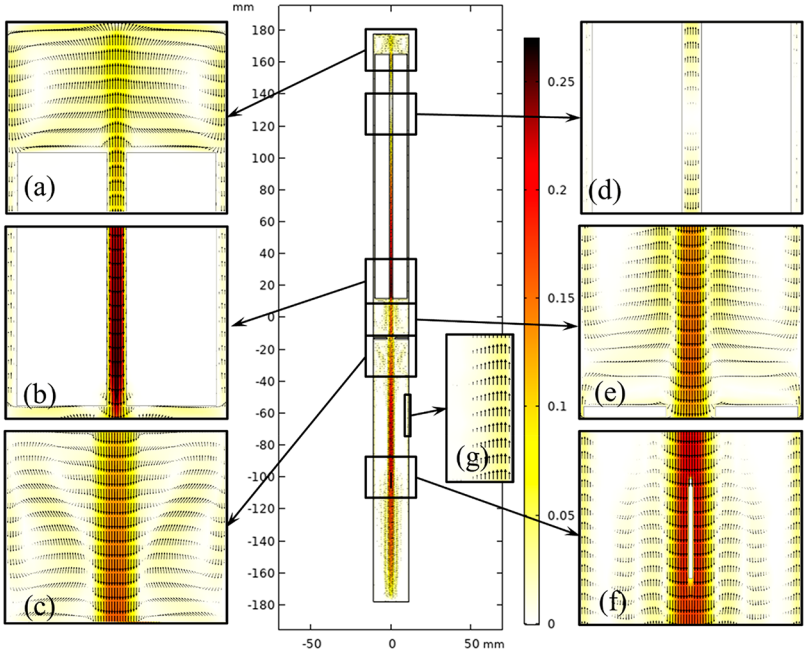

Figure 5. Velocity vector distribution in the chamber of the optimized autoclave structure. (a) Part 1. (b) Part 2. (c) Part 3. (d) Part 4. (e) Part 5. (f) Part 6. (g) Boundary layer capture.

$$C_{max} = \rho_f 11.7 \times \exp(-0.0122T)/M_{meta} \quad (13)$$

Here, M_{meta} is the molecular weight of the metastable species.

Equations 12 and (13) indicate that the GaN dissolution and crystallization rate of GaN is mainly affected by the temperature, the surface kinetics, and the concentration gradient. The temperature and the surface kinetics are the determining factors.[23,24] The GaN growth rate can be improved by increasing the species transport efficiency, which will become more important when the solubility is improved by new mineralizers.

2.3. Boundary Conditions and Numerical Setup. For the basic structure, powers of 440 and 310 W are imposed as the boundary condition for the HT heater and LT heater to maintain the external wall temperature of the lower and upper regions at the suitable values, while for the optimized structure, powers of 460 and 290 W are used to acquire the similar temperatures, because the temperature difference between the lower and upper regions is reduced by the hole in the nutrient basket. The external wall at the bottom is set insulated. Natural convection with air is used for the remaining external walls of the shell. No-slip walls are adopted for the internal walls of autoclave and baffle surfaces. The concentration source is set in the nutrient basket considering the dissolution reaction. The saturation concentration is maintained on the surface of the seed crystal depending on its temperature. The free flow and

https://doi.org/10.1021/acsomega.1c06154
ACS Omega 2022, 7, 9359−9368

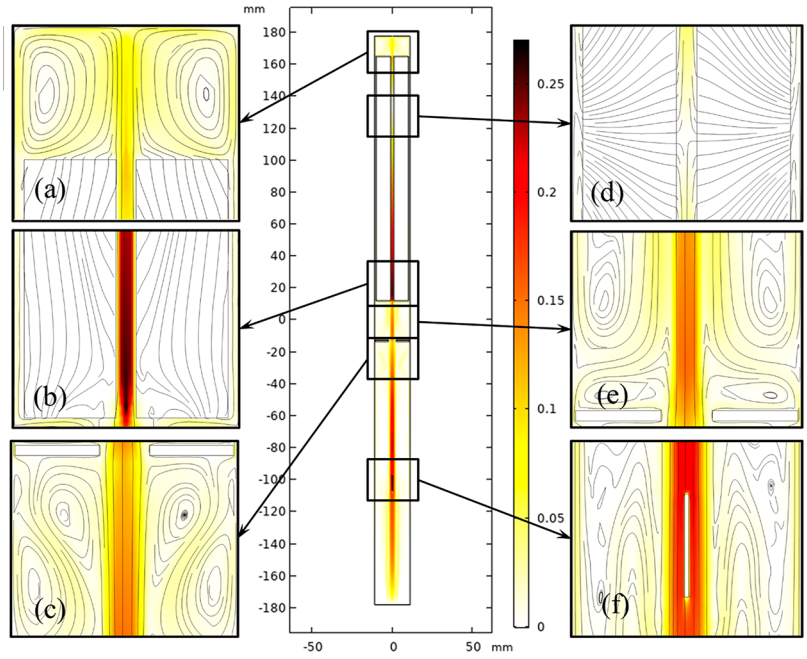

Figure 6. Streamline distribution in the chamber of the optimized autoclave structure. (a) Part 1. (b) Part 2. (c) Part 3. (d) Part 4. (e) Part 5. (f) Part 6.

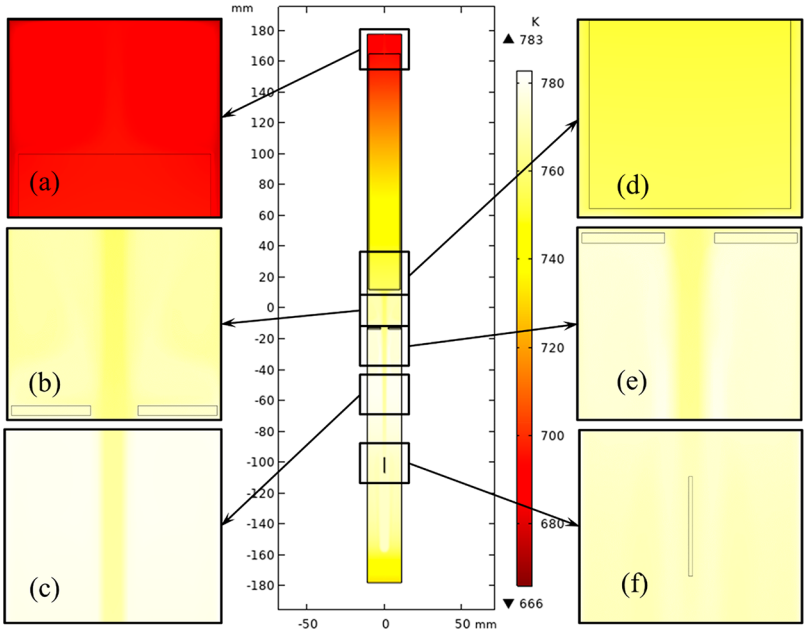

Figure 7. Temperature distribution in the chamber of the basic autoclave structure. (a) Part 1. (b) Part 2. (c) Part 3. (d) Part 4. (e) Part 5. (f) Part 6.

porous regions are coupled at the boundary. The boundary conditions can be expressed in Equations 14 and (15).

$$u_{\text{fin}} = u_{\text{fout}} \tag{14}$$

$$\mu_{\text{eff}} \frac{\partial \mathbf{u}}{\partial r}\bigg|_{\text{rin}} - \mu_{\text{f}} \frac{\partial \mathbf{u}}{\partial r}\bigg|_{\text{rout}} = \beta \frac{\mu_{\text{f}}}{\sqrt{\lambda}} \mathbf{u} \tag{15}$$

Free triangular mesh is used for the whole model. The Rayleigh number of the model is $\sim 5.0 \times 10^7$ for the model, so laminar is set for the flow region in the autoclave. Multiphysics models of Brinkman equation, porous media heat transfer, diluted material transfer in porous media, and radiative heat transfer are imposed in the COMSOL Multiphysics Software. The flow and heat transfer couple with each other to calculate the non-isothermal flow. The flow and diluted material couple with each other to calculate the concentration distribution. The heat transfer and radiative quantity couple with each other. Total elements of 27 571 and 27 582 are considered for the basic and optimized structures. A time step of 0.005 s is set for the transient calculation. It takes ~8 PC cores (PC = personal computer) and 200 h to finish the numerical simulation.

3. RESULTS AND DISCUSSION

As mentioned above, the main factors that influence the crystal growth rate are the temperature and mass transfer efficiency. The temperature field, flow field, and concentration field in this study are analyzed with different structures of the nutrient basket. The autoclave is divided into several parts to clearly show

https://doi.org/10.1021/acsomega.1c06154
ACS Omega 2022, 7, 9359−9368

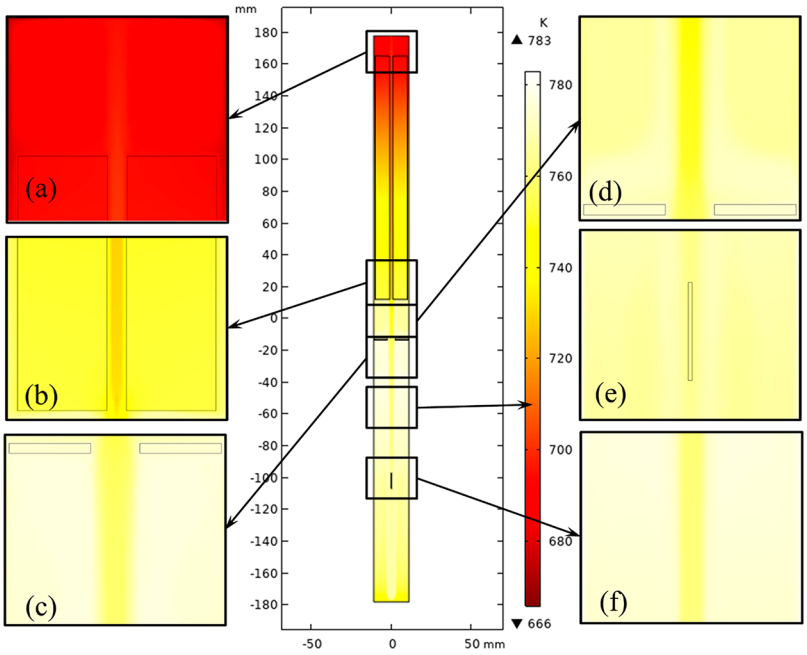

Figure 8. Temperature distribution in the chamber of the optimized autoclave structure. (a) Part 1. (b) Part 2. (c) Part 3. (d) Part 4. (e) Part 5. (f) Part 6.

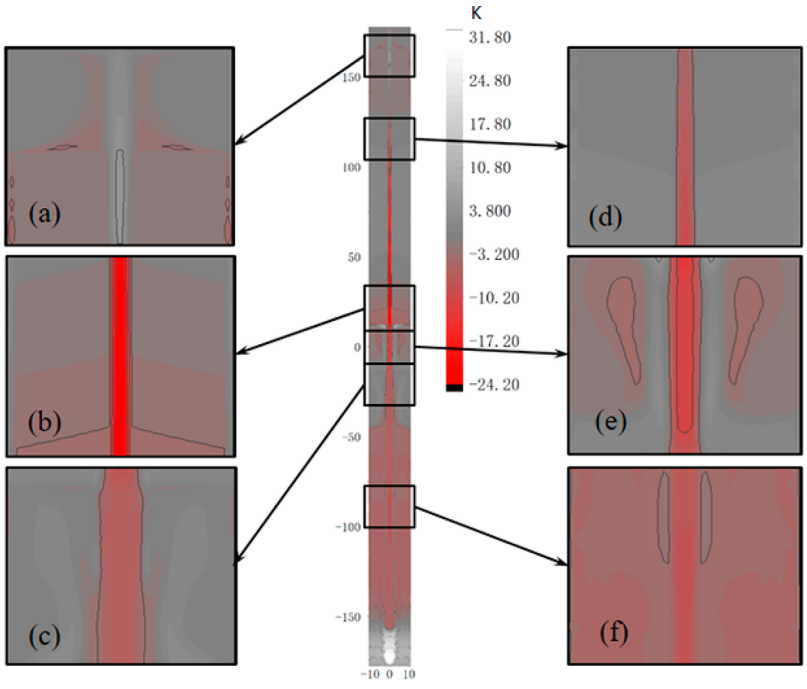

Figure 9. Temperature difference distribution in the chamber of the autoclave. (a) Part 1. (b) Part 2. (c) Part 3. (d) Part 4. (e) Part 5. (f) Part 6.

the results due to its long and narrow characteristics. Actually, there is nearly no steady state for the model because of the flow oscillation. To confirm that a quasi-steady state at which the crystal can grow well is reached, a transient simulation of 10 h is conducted.

3.1. Flow Field. Figures 3 and 4 depict the velocity and streamline field of the basic structure in the autoclave. In the upper region of the chamber, the fluid velocity is small in the porous and free-flow areas. Two vortices appear in Figure 4a. The region between the porous medium and the baffle is occupied by several eddies (Figure 4e), resulting in strong flow in this region. Most of the mass exchange is established around the interface of the porous medium and free-flow area. Recirculation of hot and cool fluid appears near the baffle. In the middle of the lower region of the chamber, there is a downward center jet, which transfers the metastable phase GaN to the seed area (Figure 4c,f). Just below the baffle, some other vortices appear before merging into the downward jet. Therefore, the effect is strengthened down the autoclave.

Figures 5 and 6 depict the flow pattern of the optimized structure. The major influence of the optimized structure is observed in the upper region of the chamber. The 2 mm

https://doi.org/10.1021/acsomega.1c06154
ACS Omega 2022, 7, 9359−9368

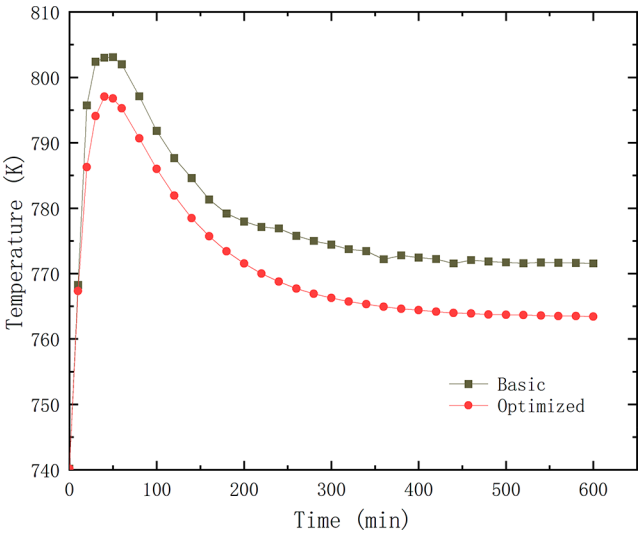

Figure 10. Average temperature variation on the seed crystal surface vs growth time.

diameter hole in the center of the nutrient basket offers a passage for the ammonia to directly access the upper region of the autoclave. The velocity obviously increases in this area, and the vortices are strengthened. On the one hand, because of the gap between the nutrient basket and the side wall, it is easier to transport mass out of this region. On the other hand, as shown for the streamline distribution (Figure 6a,d), the hole enhances the mass exchange effect by increasing the contact area of the ammonia fluid and porous medium. When comparing Figures 4e and 6e, it can be seen that the number of vortices is reduced due to the center hole. This is because the central hole in the nutrient basket offered an extra passage for the fluid. A bigger circulation is developed with the help of the extra passage. Thus, the small vortexes between the baffle and the nutrient basket are reduced. The optimized structure has little effect on the flow field in the region under the baffle.

3.2. Temperature Field. It is noteworthy that the new structure had a negative influence on the dissolution and crystallization processes. Figures 7 and 8 show the temperature distribution of the basic and optimized cases. Hot ammonia fluid from the bottom region of the chamber could attain a higher elevation due to the central hole. Accordingly, more solution can penetrate into the porous medium, resulting in a higher average temperature of the nutrient basket. Simultaneously, the temperature of the center downward jet in the bottom region of the chamber decreases. Thus, the temperature difference in the autoclave is reduced. According to ref 18, the solubility of the metastable phase GaN decreases with increasing temperature. Both phenomena are unfavorable for GaN growth. So higher HT heater power and lower LT power for the optimized structure are employed to make the nutrient basket and seed crystal work at a suitable temperature (Figure 8). Figure 9 shows the temperature difference between the optimized and basic structures. It can be seen that the values are mostly positive in the upper half and negative in the lower half, except the central area in the upper half and the bottom area in the lower half. The temperature distribution of the optimized structure is unfavorable for the crystal growth even with higher HT heater power and lower LT power when compared with the basic structure.

Figure 10 depicts the average temperature on the seed crystal surface versus growth time for the basic and optimized structures. The average temperature on the seed crystal surface of the optimized structure is lower than that of basic structure, even with a higher HT heater power and lower LT heater power. This again shows the diverse influence of the optimized structure on the temperature field.

3.3. Concentration and Supersaturation. It is well-known that the supersaturation near the seed surface is a main factor influencing the crystal growth rate.[26] The above analysis shows that the effect of the optimized structure on the flow is positive; however, its effect on the temperature field is negative. To reduce its unfavorable effect on the heat transfer, higher HT heater power and lower LT heater power are set in the autoclave.

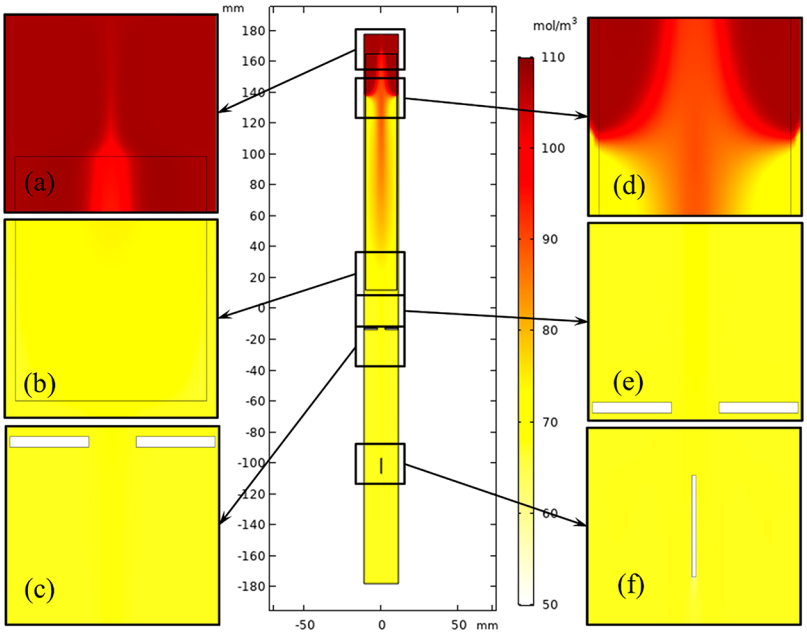

Figure 11. Concentration distribution in the chamber of the basic autoclave structure. (a) Part 1. (b) Part 2. (c) Part 3. (d) Part 4. (e) Part 5. (f) Part 6.

https://doi.org/10.1021/acsomega.1c06154
ACS Omega 2022, 7, 9359−9368

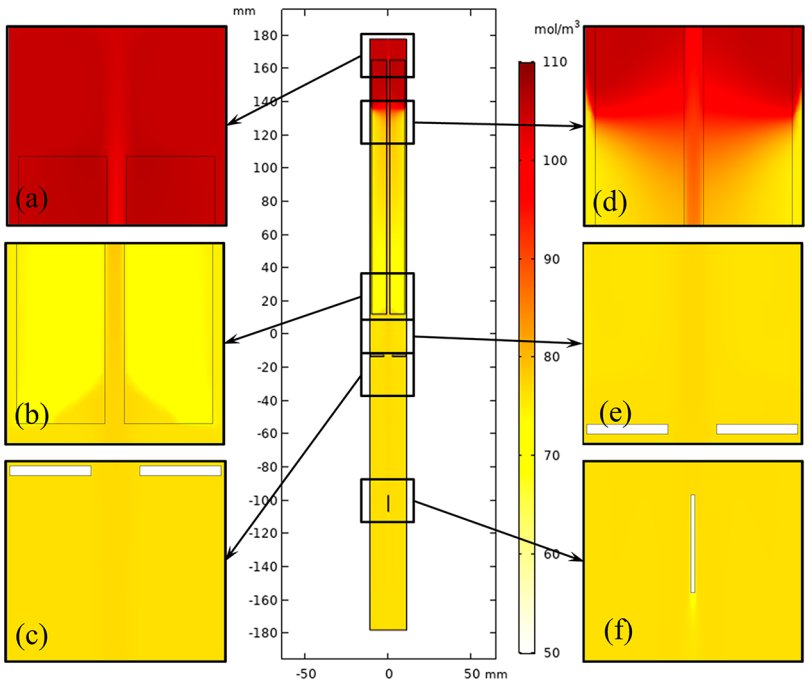

Figure 12. Concentration distribution in the chamber of the optimized autoclave structure. (a) Part 1. (b) Part 2. (c) Part 3. (d) Part 4. (e) Part 5. (f) Part 6.

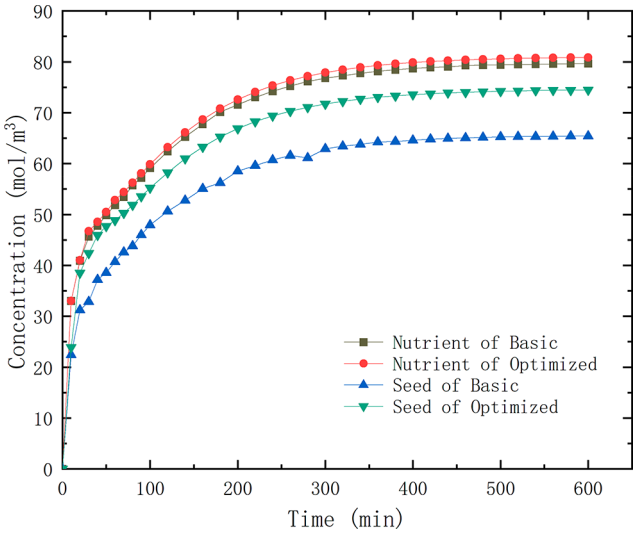

Figure 13. Average concentration of the nutrient basket and seed surface vs growth time.

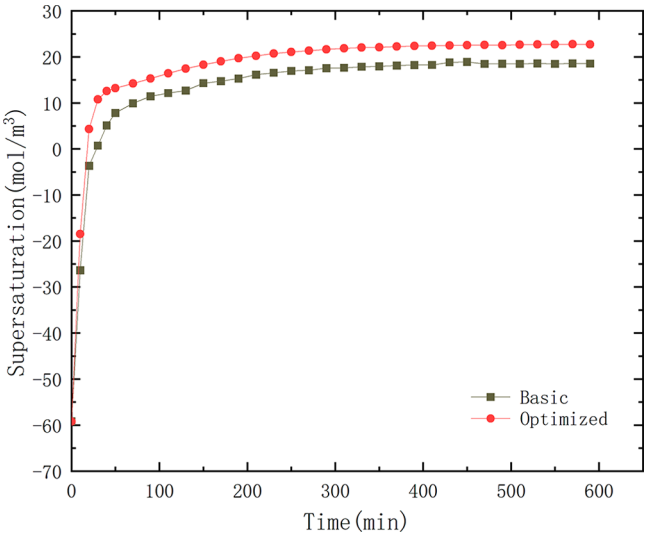

Figure 14. Average supersaturation near the seed crystal surface vs growth time.

The concentration field and supersaturation near the seed surface are calculated to analyze the acceleration of the optimized structure on the mass transfer.

Figures 11 and 12 show the concentration distribution of metastable GaN in the chambers of the basic and optimized structures. For the basic and optimized structures, the solute concentration is rather high in the upper half of the nutrient basket and between the nutrient basket and upper autoclave wall (Figure 11a). With the convection flow in the upper region of nutrient basket, the metastable GaN is transferred to the lower half of the chamber (Figures 11d and 12d). It can be clearly seen that the concentration in the lower half of the optimized structure attains a higher level than that of the basic structure.

Figure 13 depicts the concentration variation of the nutrient basket and seed crystal surface for the basic and optimized structures. It can be seen that the average concentration of the nutrient basket for the two structures is almost at the same level, while that on the seed crystal surface of the optimized structure is obviously higher. The average mass transfer efficiencies (concentration ratio of seed crystal surface and nutrient basket) are 81% and 92% for the basic and optimized structures, respectively.

Figure 14 reveals the average supersaturation versus growth time near the seed crystal surface. The supersaturation of the optimized structure is ~23% higher than that of the basic structure when reaching a steady state, which will result in a higher growth rate of the GaN crystal.

https://doi.org/10.1021/acsomega.1c06154
ACS Omega 2022, 7, 9359−9368

4. CONCLUSION

Different geometries of the nutrient basket are used to improve the growth rate in the ammonothermal method. Numerical results show that making a hole in the center of the nutrient basket is beneficial for the mass transfer in the autoclave. The mass exchange can be accelerated, and the concentration in the lower half of the autoclave is improved with the help of the central hole, despite its diverse effect on the heat transfer, which can be overcome by adjusting the heat powers. Thus, the supersaturation of metastable GaN near the seed crystal surface is increased obviously. The growth rate of the GaN crystal will be improved as well.

This study shows that the nutrient basket shape plays an important role in the heat and mass transfer in the ammonothermal system. It will be valuable to further study and optimize the geometry and structure of the nutrient basket as well as the heater power setting.

AUTHOR INFORMATION

Corresponding Author

Bing Gao − *The Institute of Technological Sciences, Wuhan University, Wuhan 430072 Hubei, China*; Email: gaobing@whu.edu.cn

Authors

Pengfei Han − *The Institute of Technological Sciences, Wuhan University, Wuhan 430072 Hubei, China*; orcid.org/0000-0001-9302-6434

Botao Song − *The Institute of Technological Sciences, Wuhan University, Wuhan 430072 Hubei, China*

Yue Yu − *The Institute of Technological Sciences, Wuhan University, Wuhan 430072 Hubei, China*

Xia Tang − *The Institute of Technological Sciences, Wuhan University, Wuhan 430072 Hubei, China*

Sheng Liu − *The Institute of Technological Sciences, Wuhan University, Wuhan 430072 Hubei, China*

Complete contact information is available at: https://pubs.acs.org/10.1021/acsomega.1c06154

Notes

The authors declare no competing financial interest.

ACKNOWLEDGMENTS

Thanks to B. Liu for his support of our research.

NOMENCLATURE

ρ_f, fluid density (kg/m^3)
u, fluid velocity (m/s)
ε, porosity
λ, permeability (m^2)
C_E, Forchheimer coefficient
μ_f, fluid viscosity (kg/(m·s))
ρ_{ref}, reference density (kg/m^3)
T, temperature (K)
T_{ref}, reference temperature (K)
β, volume expansion coefficient (1/K)
g, gravity vector (kg·m/s^2)
c_p, heat capacity (J/(kg·K))
k, thermal conductivity (W/(m·K))
Q & Q_s, heat source (W)
J_i, radiosity (W/m^3)
ε_i, emissivity
F_{ij}, view factor
$E_{b,i}$, emissive power of a blackbody (W/m^2)
q/A, heat flux (W/m^2)
C & C_f, species concentration (mol/m^3)
D, diffusion coefficient (m^2/s)
ϕ_c, mass source (mol/(m^{3}s))
$A_{fs}/\forall$, surface-to-volume fraction (1/m)
κ, reaction rate coefficient (m/s)
C_{max}, maximum concentration (mol/m^3)
M_{meta}, molecular weight of the metastable species (kg/mol)

REFERENCES

(1) Han, X. F.; Hur, M. J.; Lee, J. H.; Lee, Y. J.; Oh, C. S.; Yi, K. W. Numerical simulation of the gallium nitride thin film layer grown on 6-in. wafer by commercial multi-wafer hydride vapor phase epitaxy. *J. Cryst. Growth* **2014**, *406*, 53−58.

(2) Kucharski, R.; Sochacki, T.; Lucznik, B.; Bockowski, M. Growth of bulk GaN crystals. *J. Appl. Phys.* **2020**, *128*, 050902.

(3) Hu, J.; Wei, H. Y.; Yang, S. Y.; Li, C. M.; Li, H. J.; Liu, X. L.; Wang, L. S.; Wang, Z. G. Hydride vapor phase epitaxy for gallium nitride substrate. *J. Semicond.* **2019**, *40*, 101801.

(4) Mori, Y.; Imade, M.; Maruyama, M.; Yoshimura, M.; Yamane, H.; Kawamura, F.; Kawamura, T. *Handbook of Crystal Growth Second ed.: Bulk Crystal Growth: Basic Techniques, and Growth Mechanisms and Dynamics;* Rudolph, P., Ed.; Elsevier, 2015; pp 505−533.

(5) Mikawa, Y.; Ishinabe, T.; Kawabata, S.; Mochizuki, T.; Kojima, A.; Kagamitani, Y.; Fujisawa, H. Ammonothermal Growth of Polar and Non-polar Bulk GaN Crystal. In *Proceedings of the Conference on Gallium Nitride Materials and Devices X*, San Francisco, CA, February 9−12, 2015.

(6) Bockowski, M.; Iwinska, M.; Amilusik, M.; Fijalkowski, M.; Lucznik, B.; Sochacki, T. Challenges and future perspectives in HVPE-GaN growth on ammonothermal GaN seeds. *Semicond. Sci. Technol.* **2016**, *31*, 093002.

(7) Zajac, M.; Kucharski, R.; Grabianska, K.; Gwardys-Bak, A.; Puchalski, A.; Wasik, D.; Litwin-Staszewska, E.; Piotrzkowski, R.; Z Domagala, J.; Bockowski, M. Basic ammonothermal growth of Gallium Nitride - State of the art, challenges, perspectives. *Prog. Cryst. Growth Charact. Mater.* **2018**, *64*, 63−74.

(8) Pimputkar, S.; Kawabata, S.; Speck, J. S.; Nakamura, S. Improved growth rates and purity of basic ammonothermal GaN. *J. Cryst. Growth* **2014**, *403*, 7−17.

(9) Schimmel, S.; Duchstein, P.; Steigerwald, T. G.; Kimmel, A. C. L.; Schlucker, E.; Zahn, D.; Niewa, R.; Wellmann, P. In situ X-ray monitoring of transport and chemistry of Ga-containing intermediates under ammonothermal growth conditions of GaN. *J. Cryst. Growth* **2018**, *498*, 214−223.

(10) Letts, E.; Hashimoto, T.; Hoff, S.; Key, D.; Male, K.; Michaels, M. Development of GaN wafers via the ammonothermal method. *J. Cryst. Growth* **2014**, *403*, 3−6.

(11) Ehrentraut, D.; Pakalapati, R. T.; Kamber, D. S.; Jiang, W. K.; Pocius, D. W.; Downey, B. C.; McLaurin, M.; D'Evelyn, M. P. High Quality, Low Cost Ammonothermal Bulk GaN Substrates. *Jpn. J. Appl. Phys.* **2013**, *52*, 08JA01.

(12) Jiang, W.; Ehrentraut, D.; Downey, B. C.; Kamber, D. S.; Pakalapati, R. T.; Yoo, H. D.; D'Evelyn, M. P. Highly transparent ammonothermal bulk GaN substrates. *J. Cryst. Growth* **2014**, *403*, 18−21.

(13) Yoshida, K.; Aoki, K.; Fukuda, T. High-temperature acidic ammonothermal method for GaN crystal growth. *J. Cryst. Growth* **2014**, *393*, 93−97.

(14) Chen, Q. S.; Prasad, V.; Chatterjee, A.; Larkin, J. A porous media-based transport model for hydrothermal growth. *J. Cryst. Growth* **1999**, *198*, 710−715.

(15) Chen, Q. S.; Pendurti, S.; Prasad, V. Effects of baffle design on fluid flow and heat transfer in ammonothermal growth of nitrides. *J. Cryst. Growth* **2004**, *266*, 271−277.

https://doi.org/10.1021/acsomega.1c06154
ACS Omega 2022, 7, 9359−9368

(16) Chen, Q. S.; Pendurti, S.; Prasad, V. Modeling of ammonothermal growth of gallium nitride single crystals. *J. Mater. Sci.* **2006**, *41*, 1409−1414.
(17) Masuda, Y.; Suzuki, A.; Mikawa, Y.; Kagamitani, Y.; Ishiguro, T.; Yokoyama, C.; Tsukada, T. Numerical simulation of GaN single-crystal growth process in ammonothermal autoclave - Effects of baffle shape. *Int. J. Heat Mass Transfer* **2010**, *53*, 940−943.
(18) Kakhki I, M. *Comprehensive computational investigation of gallium nitrite ammonothermal crystal growth [D];* University of Massachusetts Lowell, 2015.
(19) Schimmel, S.; Kobelt, I.; Heinlein, L.; Kimmel, A. C. L.; Steigerwald, T. G.; Schlucker, E.; Wellmann, P. Flow Stability, Convective Heat Transfer and Chemical Reactions in Ammonothermal Autoclaves-Insights by In Situ Measurements of Fluid Temperatures. *Crystals* **2020**, *10*, 723.
(20) Enayati, H. Effect of Reactor Size in a Laterally-Heated Cylindrical Reactor. *Int. J. Heat Technol.* **2020**, *38*, 275−284.
(21) Enayati, H.; Chandy, A. J.; Braun, M. J.; Horning, N. 3D large eddy simulation (LES) calculations and experiments of natural convection in a laterally-heated cylindrical enclosure for crystal growth. *Int. J. Therm. Sci.* **2017**, *116*, 1−21.
(22) Pendurti, S.; Chen, Q. S.; Prasad, V. Modeling ammonothermal growth of GaN single crystals: The role of transport. *J. Cryst. Growth* **2006**, *296*, 150−158.
(23) Shibata, H.; Waseda, Y.; Ohta, H.; Kiyomi, K.; Shimoyama, K.; Fujito, K.; Nagaoka, H.; Kagamitani, Y.; Simura, R.; Fukuda, T. High thermal conductivity of gallium nitride (GaN) crystals grown by HVPE process. *Mater. Trans.* **2007**, *48*, 2782−2786.
(24) Laidler, K. J. THE DEVELOPMENT OF THE ARRHENIUS EQUATION. *J. Chem. Educ.* **1984**, *61*, 494−498.
(25) Wang, B. G.; Callahan, M. J.; Rakes, K. D.; Bouthillette, L. O.; Wang, S. Q.; Bliss, D. F.; Kolis, J. W. Ammonothermal growth of GaN crystals in alkaline solutions. *J. Cryst. Growth* **2006**, *287*, 376−380.
(26) Carbonell, R.; Whitaker, S. Heat and mass transfer in porous media. In *Fundamentals of Transport Phenomena in Porous Media;* Bear, J., Corapcioglu, M. Y., Eds.; Springer Netherlands, 1984; pp 121−198.

https://doi.org/10.1021/acsomega.1c06154
ACS Omega 2022, 7, 9359−9368